Journal of Nuclear Medicine, published on October 8, 2015 as doi:10.2967/jnumed.115.157677

Promising future: Comparable Imaging Capability of MRI compatible SiPM and Conventional Photo-sensor Based Preclinical PET Systems*

Aron K. Krizsan[1], Imre Lajtos[1], Magnus Dahlbom[2], Freddie Daver[3], Miklos Emri[1], Sandor A. Kis[1], Gabor Opposits[1], Laszlo Pohubi[1], Norbert Potari[1], Gyula Hegyesi[4], Gabor Kalinka[4], Janos Gal[4], Jozsef Imrek[4], Ferenc Nagy[4], Ivan Valastyan[4], Beata Kiraly[4], Jozsef Molnar[4], Delfo Sanfilippo[5], Laszlo Balkay[1]

[1]*Department of Nuclear Medicine, Medical Center, University of Debrecen, Hungary;*

[2]*Ahmanson Biological Imaging Center, Department of Molecular and Medical Pharmacology, David Geffen School of Medicine at University of California at Los Angeles, USA*

[3]*Alfred Mann Institute for Biomedical Engineering, University of Southern California, USA*

[4]*Institute for Nuclear Research, Hungarian Academy of Sciences, Debrecen, Hungary;*

[5]*ST Microelectronics, Catania, Italy;*

Responsible author: Aron Krisztian Krizsan, 4032 Debrecen, Nagyerdei krt. 98. Hungary, Tel: +36203937068, Fax: +3652255500, aron.krizsan@gmail.com

Word Count: 4949 words

Disclosure:

This work was supported under the project 'Central Nervous System Imaging' by the Hungarian National Development Agency (No. ENIAC_08-1-2011-0002) and by the ENIAC Joint Undertaking (No. 120209). This research was supported by the European Union and the State of Hungary, co-financed by the European Social Fund in the framework of TÁMOP-4.2.4.A/ 2-11/1-2012-0001 'National Excellence Program'.

*Short running title: Compare SiPM and PMT based preclinical PET

We have recently completed construction of a new preclinical PET system, the MiniPET-3, which utilizes state-of-the-art Silicon Photomultiplier (SiPM) photo-sensor technology, making possible dual modality imaging with MRI. In this article, we compare the imaging capabilities of two small animal imaging systems with the same crystal geometry but different photo-sensors: SiPM used on the MiniPET-3 and the conventional Photomultiplier Tubes (PMTs) for MiniPET-2. **Methods:** The standard measurements proposed by the National Electrical Manufacturers Association (NEMA) NU 4 were performed on both MiniPET systems. These measurements included the determination of spatial resolution, system sensitivity, energy resolution, count rate performance, scatter fraction, spill-over-ratio (SOR) for air and water, recovery coefficients (RC), and image uniformity. Energy windows were set to 350-650 keV and 360-662 keV on the MiniPET-2 and MiniPET-3 scanners respectively. **Results:** The spatial resolution of the MiniPET-3 was approximately 17% better on average compared to the MiniPET-2. Both scanners showed similar performance in terms of peak absolute sensitivity (~1.37%), SOR air (~0.15), SOR water (~0.25), and RC (~0.33, 0.59, 0.81, 0.89, 0.94). Uniformity was measured to be 5.59% and 6.49% for the MiniPET-2 and MiniPET-3 respectively. Minor differences were found in scatter fraction. When using the rat-like phantom, the Noise Equivalent Count Rate (NECR) peak on the MiniPET-2 was measured as 14 kcps, while on the MiniPET-3 it was 24 kcps. However, when using a mouse-like phantom, these values were 55 kcps and 91 kcps for the MiniPET-2 and MiniPET-3 respectively. The optimal coincidence time window was found to be 6 ns for the MiniPET-2 and 8 ns for the MiniPET-3. **Conclusion:** Our results indicate that, the overall imaging performance of the SiPM-based MiniPET-3 preclinical PET scanner produces images of similar quality than the conventional PMT based technology (MiniPET-2) for small animal imaging.

Key words: MiniPET; small-animal PET scanner; performance evaluation; instrumentation; molecular imaging

The efforts to combine PET and MRI into an integrated system achieved important advancements in the recent years, mainly fostered by new photo-sensor technologies (*1-4*). Conventional PMT detectors benefit from high signal gain in the range of 10^5 - 10^7 (*5, 6*). Low noise and fast transit time (~100 ps) are also available today, and has made this photo-sensor the first candidate for application involving the Time Of Flight (TOF) PET technology. In addition, PMTs have lower noise compared to the Avalanche Photodiodes (APDs) or SiPM detectors (*5*). However, in strong magnetic fields PMT technology is not able to produce acceptable position maps for imaging purposes. In contrast, APDs can be used efficiently as a photo-sensor for PET when near strong magnets. Some successful approaches using APDs have already been introduced for combined PET/MRI applications (*2, 7, 8*). However, APDs have a significantly higher rise times (up to 2-3 ns) (*5*) that prevent adequate timing resolution for TOF. The low gain (~10^2) is also a disadvantage of APDs (*2, 5*).

Coupling LSO crystals with new SiPM technology, timing resolution sufficient for TOF measurements has already been reached (*9*). The considerably lower noise of SiPMs (compared to the APDs) and high gain (~10^6) are additional promising features of SiPM, which makes this technology suitable for PET photo-detectors in high magnetic field environments. Some approaches for the inclusion of SiPM in a full-ring PET detector system have already been introduced (*4, 10, 11*). A new preclinical PET scanner, the MiniPET-3, was developed at our institutions recently, based on the former gantry parameters of MiniPET-2 (*12*) with Lutetium-Yttirium Oxyortosilicate (LYSO) crystal detectors. However, the conventional PMT detectors of MiniPET-2 were replaced with SiPM technology (ST Microelectronics) for use in the MiniPET-3. In addition, the readout boards have been slightly altered in terms of signal encoding of SiPM and PMT, while the scintillation crystal geometry in the gantry remained the same for both systems.

Since the only significant difference between the two scanners is the detector technology, the systems provide us a method to compare the imaging capabilities and system performance of the new MRI compatible SiPM photo-sensors (on the MiniPET-3) and the conventional PMTs (on the MiniPET-2). Within this study, the direct comparison was performed by measurements as specified in the NEMA NU 4 protocols without the operation in MRI high magnetic fields.

MATERIALS AND METHODS

Scanner Description

The technical and geometrical parameters both MiniPET scanners are listed in Table 1. The two systems include the same-sized gantry, detector crystal material, crystal size, crystal pitch and detector module configuration. The significant difference between the systems lies in the photo-sensors: the MiniPET-2 system includes conventional PMTs, while the MiniPET-3 system includes SiPMs and a readout system optimized for this type of detectors. A row-column readout of the SiPM matrix was used without applying individual signal processing channels to each matrix element. Weighting circuits were

connected directly to the row and column outputs as proposed by Y. Wang et al. (*13*), but modified in such a way as to reduce the dark noise. The overlap between the crystals and the SiPM sensitive areas were determined during the design of the SiPM sensors for the purpose of optimal position encoding. The LYSO crystal matrix and the SiPM sensor board were attached together with a light-guide designed to receive light from every scintillation crystal. SiPM sensors were arranged to overlap with crystal clusters of three rows and three columns. Light from these clusters was collected at a relatively high efficiency compared to crystal elements, which did not overlap with the SiPM as shown in Figure 1. Among all crystal elements, 59.5% were located at regions of relatively high light collection efficiency, while 40.5% were located in regions of relatively low light collection efficiency. A total of 324 SiPM sensors (18x18) were arranged in 2x2 blocks, and these quads were produced in a 9x9 configuration. The SiPM matrix active area is 48x48 mm^2 and the size of each SiPM sensor is 1.95x2.2 mm^2. The number of microcells in each sensor is 833. An epoxy light guide (Philips Research, Eindhoven) was used between the SiPM tile and the crystal matrix with a thickness of 1.3 mm. In the case of MiniPET-2, the PMTs were attached to the LYSO scintillation crystal matrixes with a special optical coupling compound called Visilox V-788. In this case the thickness of the optical coupling remained under 0.5 mm. Digital signals were fed into a Xilinx Vertex4 Field Programmable Gate Array (FPGA) board, where time stamp generation, energy calculation, signal recognition and status check processes took place (*12*). Data from the detector modules were transmitted to the data acquisition computer via the 100BASE-TX Ethernet network system. The custom made MultiModal Medical Imaging (M3I) software library was developed (*14*) for the tasks of data collection and processing such as primary data processing, scanner calibration, image reconstruction, image processing and evaluation of performance parameters. This software tool arranges the data into 3D Line Of Response (LOR) or single events list-mode data files that can be histogrammed into 2D sinograms. The M3I performs 2D Maximum Likelihood Expectation Maximization (ML-EM) (*15*) that we used in case of the image quality measurements. For the evaluation of spatial resolution of the systems, Filtered Backprojection (FBP) was used. All other images in this evaluation were reconstructed using ML-EM, as implemented in M3I, using 20 iterations without any post-reconstruction filtering. The same system matrix was used for both systems during this study.

Position encoding and energy resolution

Measurements performed for position encoding and energy resolution were conducted with an ^{18}F point source of 4 MBq activity, while positioned in the center of the Field of View (FOV) axially and transaxially. A 1200 sec list mode dataset was acquired in each case. From the list-mode data, events were sorted into energy histograms for every crystal element, and the Full Width at Half Maximum (FWHM) values of the 511 keV peaks were calculated. The ^{18}F energy resolution was calculated as the FWHM value divided by the peak channel number times 100. Measurements performed on the MiniPET-3 took into account the non-linearity between SiPM signals and photon energies. The lower energy threshold was set to 360 keV

using ^{131}I measurements, while the upper energy threshold to 662 keV with ^{137}Cs. These isotopes have definite signal peaks at the mentioned energies. For position encoding purposes this same measurement protocol was used, and the position maps for each detector modules were determined.

Coincidence Time Window Optimization

An optimal coincidence time window (τ-value) must balance the need to maximize the true coincidence count rate while minimizing the randoms count rate. This optimization is dependent on the source activity as well as the FWHM of the coincidence time histogram. In order to determine the optimal τ-value on the MiniPET-3, a cylinder phantom (inner diameter: 45 mm, length: 200 mm) filled with ^{68}Ga was used. Raw data was acquired at an initial activity level of 17.05 MBq for two-minutes using a τ-value of 2 ns. Nineteen subsequent measurements were repeated with increasing the τ-value in 2 ns increments, resulting in a total of 20 measurements. The actual true and random coincidence rates were obtained during the measurement. In addition, we calculated a parameter that is similar to NEC defined as: True^2/(True+2*Random), which was used to find the optimal τ-value. For the MiniPET-2 the optimal τ-value was determined in a previous study (*12*). Each detector module is in coincidence with 3 other modules on the opposite side of the gantry. Time alignment for all 18 detector-connections were performed with appropriately shifting the coincidence time histograms in case of both MiniPET systems.

Spatial Resolution

The spatial resolution for both the MiniPET systems was measured using a 1 x 1 x 1 cm cast acrylic cube (Eckert & Ziegler Isotope Products Inc.). The center of the cube included a 0.25 mm^3 spherical ^{22}Na point source. Individual measurements using this point source were performed at separate locations: 0 mm, 5mm, 10mm, 15mm, 25mm and 35 mm radial offset from the central axis of the scanner. These measurements were repeated using the same radial locations, but shifted to ¼ from the axial center. The 3D data were then re-binned into 2D LORs using the Single-Slice Rebinning (SSRB) algorithm. As proposed by the NEMA standard, we used 2D FBP for the image reconstructions of the spatial resolution acquisitions. For each of the 12 measurements, a profile through the point was obtained. The FWHM of this profile was then used to determine the spatial resolution for each image.

Sensitivity

The sensitivity measurement was performed using a ^{22}Na point source initially placed in the center of the FOV. Subsequent images were taken by shifting the point source axially towards the edge of the detector ring in 1.35 mm increments, resulting in a total of 35 scans. The absolute sensitivity for each *i*th (i=1, 2… 35) acquisition was calculated as:

$$S_{A,i} = \frac{1}{0.905}\left(\frac{R_i - R_{B,i}}{A_{cal}}\right) \times 100\% \quad \text{Eq. 1}$$

where A_{cal} is the activity of the point-source, 0.905 is the branching ratio of ^{22}Na, R_i and $R_{B,i}$ are the source and background total count rate for the *i*th acquisition, respectively. System peak absolute sensitivity is defined as the $S_{A,i}$ at the center of FOV (*13*). Total Absolute Sensitivity ($S_{A,tot}$) was calculated using the following equation:

$$S_{A,tot} = \frac{\sum_{i=1}^{n} S_{A,i}}{n} \quad \text{Eq. 2}$$

where, $S_{A,i}$ is the absolute sensitivity at slice *i*, *n* is the maximal slice index (35 in our case) (*12*). This formula follows the concept of some recent articles (*12*, *16*, *17*) and the extension of the NEMA NU-4 in 2011.

Image Quality Phantom Study

For the image quality measurements, the NEMA NU4 IQ phantom was used, which has a cylindrical shape with fillable rods of different diameters drilled in cold, solid background for computing RC values. In addition to RC, the NEMA standard also includes protocols for the determination of image uniformity and SORs using a homogenous region and two cylindrical chambers (cold chambers) within the IQ phantom. The uniformity is calculated as percent Standard Deviation (%STD) that equals to Ustd/Umean*100%, where Umean and Ustd are the mean and standard deviation values for the homogenous region. Image acquisition, histogramming, and reconstruction were very similar when performed on the MiniPET-2 and MiniPET-3. These images were acquired from the NU 4 IQ phantom filled with ^{18}F at an initial activity of 3.7 MBq activity. One of the cold chambers was filled with water, the other with air. The phantom was positioned on the animal bed port of the scanner along its central axis. Data was acquired using 1200 sec list-mode dataset of the phantom was acquired in both cases. The list-mode raw data were binned into 3D coincidence lines-of-responses (LORs), representing in the geometry of the scanner. These 3D data were then re-binned into 2D LORs using the Single-Slice Rebinning (SSRB) algorithm. Images were reconstructed from the 2D rebinned data using the ML-EM method with 20 iterations. From the reconstructed images RC, SOR and uniformity values were determined using our cross validated software.

Scatter Fraction and Count Rate Performances

The count rate protocol allows the determination of the true and random ratio, as well as the NEC rate. The scatter fraction was determined from the data measured at low activity levels when the random ratio is negligible. The measurements were performed using two cylindrical scattering phantoms (the so called rat and mouse phantoms) with a line source insert of high activity concentration, as recommended by the NEMA NU 4 standard.

RESULTS

Position encoding and energy resolution

The flood field images of both MiniPET scanners are shown in Figure 2. These images illustrate the difference between the position mapping capabilities of the LYSO crystal elements when used with PMTs versus SiPM detectors. Although the position map of MiniPET-2 seems to be more homogenous, fewer crystals can be identified at the border area. On the other hand, non-uniform patterns can be seen in the MiniPET-3 position maps. This effect is due to the periodically changing overlaps between the crystal elements and the sensitive area of SiPMs. Moreover, some of the crystal elements are arranged in 3x3 clusters overlapping the SiPM sensors, while other crystal elements are located in between the sensitive areas of SiPM sensors. Two representative profiles from both MiniPET-2 and MiniPET-3 position maps are shown in Figure 2. The average top/valley (T/V) ratios for the MiniPET-2 and MiniPET-3 detector modules are 5.20±0.21 and 5.73±1.03, respectively. The highest T/V of the MiniPET-3 is more pronounced if we consider only the crystals in the high light collection position. In this case the average T/V is 6.6±0.43. The energy spectra for each crystal position were also investigated and the related energy resolutions were calculated. For both MiniPET systems the energy resolution value related to each crystal element in case of two representative detector modules are displayed (Figure 1.B and C). The system average energy resolution values were measured to be 19.98±7.59 % and 31.74±11.30 % for the MiniPET -2 and MiniPET-3 respectively. The energy resolution pattern of the MiniPET-3 correlates well with the flood field image. Furthermore, the energy resolutions are higher for the crystal positions with high light collection and lower for the crystal positions with low light collection.

Coincidence Time Window Optimization, Spatial Resolution and Sensitivity

The coincidence time window data illustrates that the plateau of the true coincidence rate starts between 8 ns and 12 ns (Fig. 3); however the random coincidence rate is reasonably low within this range. The NEC-like measure had a maximum value close to 8 ns as observed on Figure 3. Therefore, the default τ-value was set to 8 ns to keep the random/true coincidence rate as low as possible near the close-to-optimal true event rate. In the case of the MiniPET-2 system, the optimal τ-value was found to be 6 ns based on former measurements (*12*).

Spatial resolution was also measured using the FWHM of the radial, axial and tangential profiles as a function of radial distance from the axial center for MiniPET-2 and MiniPET-3 scanners at the ¼ offset from the axial center as seen in Figure 4. These values were found to be about 17% better, on average, for the MiniPET-3 system compared to the MiniPET-2. The minimal value of spatial resolution for all three directions (radial, tangential, axial) is approximately 1.35 mm for the MiniPET-2 at the center, increasing to 2.33 mm at the radial edge. On the other hand, the minimal spatial resolution of the MiniPET-3 was approximately 1.15 mm and increased to 1.87 at the radial edge. The effective transaxial FWHM spatial resolution proposed by Goertzen et al. (*16*) was found to be 1.34 mm and 1.25 mm for the MiniPET-2 and MiniPET-3 scanners, respectively. The axial absolute sensitivity profiles were also calculated as recommended in the NEMA-NU4. These results were similar for both systems. The peak absolute sensitivity and the total absolute sensitivity ($S_{A,\ tot}$) data are summarized in Table 2 for both MiniPET scanners.

Image Quality Phantom Study, Scatter Fraction and Count Rate Performances

Three different sections of the NU-4 IQ phantom for both MiniPET-systems are displayed (Fig. 5A and B): the fillable rods (left); uniform cylinder (center); and the water and air chambers (right). Note that the smallest rod is more visible in image acquired with the MiniPET-3 compared to that of the MiniPET-2. The SOR values found to be similar for both systems (~0.15 and ~0.25), while the uniformity was 5.59% in the case of MiniPET-2 and 6.49% in case of MiniPET-3 (Table 2). RC values showed comparable results for both of the MiniPET systems, while four rods showed slightly higher values in case of the MiniPET-3 (Fig. 5C).

The NEC rate of the MiniPET-3 performs higher (better) than for the MiniPET-2, while the scatter fraction is slightly lower for the MiniPET-3 for both of the phantoms (Table 2). The count rate performances of the MiniPET-2 and MiniPET-3 scanners are displayed in the supplemental material (Supplemental Figure A and B) measured with the larger phantom geometry. However, we observed that the total count rate performances have a maximum around 50 MBq activity level for both scanners, but the maximum accepted NEC count is approximately twice as high for the MiniPET-3 (Fig 6.).

DISCUSSION

There have been many successful attempts for merging MRI systems with PET systems in recent years (*4, 9-11*). Some have reported on the performance parameters of SiPM-based full ring preclinical PET scanners or MRI inserts (*4, 10, 18, 19*). However, only some of the NEMA NU 4 measurement protocols have been carried out on these systems. For a comprehensive comparison between a SiPM-based preclinical PET system and a conventional PMT-based system we

performed all the necessary measurements recommended by the NEMA NU 4 standard on both MiniPET scanners. Comparison was facilitated by the fact that the SiPM-based MiniPET-3 and the PMT-based MiniPET-2 share nearly identical scintillation crystal geometry. Dark noise problems can be minimized if each SiPM matrix element has an individual signal-processing channel (*4, 10, 11*) but this solution would need a tremendous number of electronic channels. To reduce the number of channels, a special readout arrangement was developed in row-column manner for the SiPM matrix. In addition, appropriate weighting circuits were directly connected to the row and column outputs, allowing the 81 SiPM signals to be decoded into four outputs.

From the flood-field images one can conclude that the MiniPET-3 performs about 1.5 times better in terms of peak-to-valley ratios compared to the MiniPET-2. In addition, discrepancies in light sharing for the two photo-detectors may explain the performance differences in spatial resolution between the two systems. Moreover, the MiniPET-3 exhibits superior axial, radial, and tangential spatial resolutions. This improvement is even more pronounced as the source is moved towards the radial edges. The overall axial system sensitivity shows similar characteristics between the systems as expected from the nearly identical scintillation crystal material and geometry. The image quality study is currently used as the gold standard for determining imaging characteristics of many preclinical PET systems (*8, 12, 16, 20, 21*), and showed similar results in terms of RC and SOR values for both MiniPET scanners. Better spatial resolution results in noisier images for the same number of counts, which explains the worse uniformity for the MiniPET-3 system. The NEC count rate peak values occur at similar activity levels, around 50 MBq for both scanners, however, these values are lower for the MiniPET-2. This is primarily because of the significantly higher dead time factor for the MiniPET-2 (680 ns) versus the MiniPET-3 (250 ns). The inferior dead time of the MiniPET-2 is a result of differences of the front-end electronics in the pulse shaping of the front-end preamplifiers as well as digital processing of each signal. The calculated scatter fractions from both the rat-sized and mouse-sized phantom experiments show comparable results, while the MiniPET-3 performs slightly better and that correlates with the somewhat better SOR values (Table 2). This seems to contradict the fact that the energy resolutions for the two systems are not the same. Indeed, the average energy resolution is about 32% (instead of 20%) for the SiPM-based system, 60% worse compared to the PMT-based system. One reason for this discrepancy is that, the calculated SF defined by the NEMA NU 4 protocol does not represent all the scattered events. In fact, it only includes only the photons scattered in the body. In addition, for preclinical PET scanners the number of scatters is definitely higher in the scintillation crystal than in the tissue (about 50% vs 10%) (*22*), thus the energy blurring has even less effect. A second explanation for the surprising scatter fraction results is that, no significant correlation could be found between the SF and the energy resolution in case of other preclinical systems (*16*). The main disadvantage of the MiniPET-3 compared to the MiniPET-2 is the known dependence on ambient temperature of the semiconductor-based detectors (*23, 24*). A limitation of this study is that we did not take into account the performance of the scanners in high magnetic fields. However, other research groups have proved the stability and proper performance of

SiPMs in MRI systems already (*18, 19*). Although both MiniPET systems have a relatively small FOV compared to other preclinical PET scanners (*16, 21, 25*), the main goal of this study was to compare SiPM with PMT technology while scanner scintillation crystal geometries, system matrices, slice rebinning algorithms, and even image reconstructions are kept identical.

CONCLUSIONS

The main imaging capabilities of the SiPM based MiniPET-3 small animal PET scanner does not differ significantly from that of the conventional PMT photodetector based MiniPET-2 scanner. Based on these results we can conclude that the MRI-compatible SiPM-based MiniPET-3 scanner shows comparable results with the conventional technology producing images of high quality for small animal imaging.

ACKNOWLEDGMENTS

The authors would like to express special thanks to Darrel Hathcock, Russel Chun and Attila Forgacs for their contributions and thoughtful conversations during the period of these measurements and evaluations.

REFERENCES

1. Judenhofer MS, Wehrl HF, Newport DF, et al. Simultaneous PET-MRI: a new approach for functional and morphological imaging. *Nature Med.* 2008;14:459-465.
2. Pichler BJ, Judenhofer MJ, Catana C, et al. Performance test of an LSO-APD detector in 7-T MRI scanner for simulataneous PET/MRI. *J Nucl Med*. 2006;47:639-647.
3. Vaska P, Cao T. The state of instrumentation for combined positron emission tomography and magnetic resonance imaging. *Semin Nucl Med*. 2013;43:11–18.
4. Weissler B, Gebhardt P, Lerche CW, et al. MR compatibility aspects of a silicon photomultiplier-based PET/RF insert with integrated digitization. *Phys Med Biol.* 2014;59:5119–5139.
5. Lecomte R. Novel detector technology for clinical PET. *Eur J Nucl Med Mol Imaging* 2009;36(Suppl 1):S69–S85.
6. Phelps ME. PET, Molecular Imaging and Its Biological Applications. In: Cherry S, Dahlbom M, eds. *PET: Physics, Instrumentation and Scanners.* Springer; 2004: 20, 99.
7. Judenhofer MS, Cherry SR. Applications for preclinical PET/MRI. *Semin Nucl Med* 2013;43:19-29.
8. Prasad R, Ratib O, Zaidi H. NEMA NU-04-based performance characteristics of LabPET-8^{TM} small animal PET scanner. *Phys Med Biol.* 2011;56:6649-6664.
9. Aguilar A, Gracia-Olcina R, Martinez PA, et al. Time of flight mesurements based on FPGA and SiPMs for PET-MR. *Nucl Instrum Meth A.* 2014;734:127–131.
10. Lu Y, Yang K, Zhou K, Zhang Q, Pang B, Ren Q. Development of a SiPM-based imaging system for small animals. *Nucl Instrum Meth A.* 2014;743: 30–38.
11. Espana S, Marcinkowski R, Keerman V, Vandenberghe S, Van Holen R. DigiPET: sub-millimeter spatial resolution small-animal PET imaging using thin monolithic scintillators. *Phys Med Biol*. 2014;59:3405-3420.
12. Lajtos I, Emri M, Kis SA, et al. Performance evaluation and optimization of the MiniPET-II scanner. *Nucl Instrum Meth A.* 2013;707:26–34.
13. Wang Y, Zhang Z, Li D, et al. Design and performance evaluation of a compact, large-area PET detector module based on silicon photomultipliers. *Nucl Instrum Meth A.* 2012;670:49-54.
14. MI3Library, http://minipetct.com
15. Hudson HM, Larkin RS. Accelerated image reconstruction using ordered subsets of projection data. *IEEE Trans Med Imag.* 1994;13:601-609.
16. Goertzen AL, Bao Q, Bergeron M, et al. NEMA NU4-2008 Comparison of preclinical PET imaging systems. *J Nucl Med*. 2012;53:1300-1309.

17. Visser EP, Disselhorst JA, Brom M, et al. Spatial resolution and sensitivity of the Inveon small-animal PET scanner. *J Nucl Med.* 2009;50:139-147.
18. Yoon HS, Ko GB, Kwon SI et al. Initial results of simultaneous PET/MRI experiments with an MRI-compatible Silicon Photomultiplier PET scanner. *J Nucl Med.* 2012;53:608-614.
19. Wehner J, Weissler B, Dueppenbecker P, et al. PET/MRI insert using digital SiPMs: Investigation of MR-compatibility. *Nucl Instrum Meth A.* 2014;734:116-121.
20. Disselhorst JA, Brom M, Laverman P, et al. Image-quality assessment for several positron emitters using the NEMA NU 4-2008 standards in the Siemens Inveon small-animal PET scanner. *J Nucl Med.* 2010;51:610-617.
21. Szada I, Mackewn J, Patay G, et al. National Electrical Manufacturers Association NU-4 Performance Evaluation of the PET Componenet of the NanoPET/CT Preclinical PET/CT Scanner *J Nucl Med*. 2011;52:1741–1747.
22. Lajtos I, Czernin J, Dahlbom M, et al. Cold wall effect eliminating method to determine the contrast recovery coefficient for small animal PET scanners using the NEMA NU-4 image quality phantom. *Phys Med Biol*. 2014;59:2727-2746.
23. Keereman V, Van Holen R, Vandenberghe S, Vanhove C. Temperature dependence of APD-based PET scanners. *Med Phys.* 2013;40:092506-1-092506-13.
24. Roncali E, Cherry S. Application of silicon photomultipliers to positron emission tomography. *Ann Biomed Eng*. 2011;39:1358–1377.
25. Bao Q, Newport D, Chen Mu, Stout DB, Chatziioannou AF. Performance evaluation of the Inveon dedicated PET preclinical tomograph based on the NEMA NU4 standards. *J Nucl Med*. 2009;50:401–408.

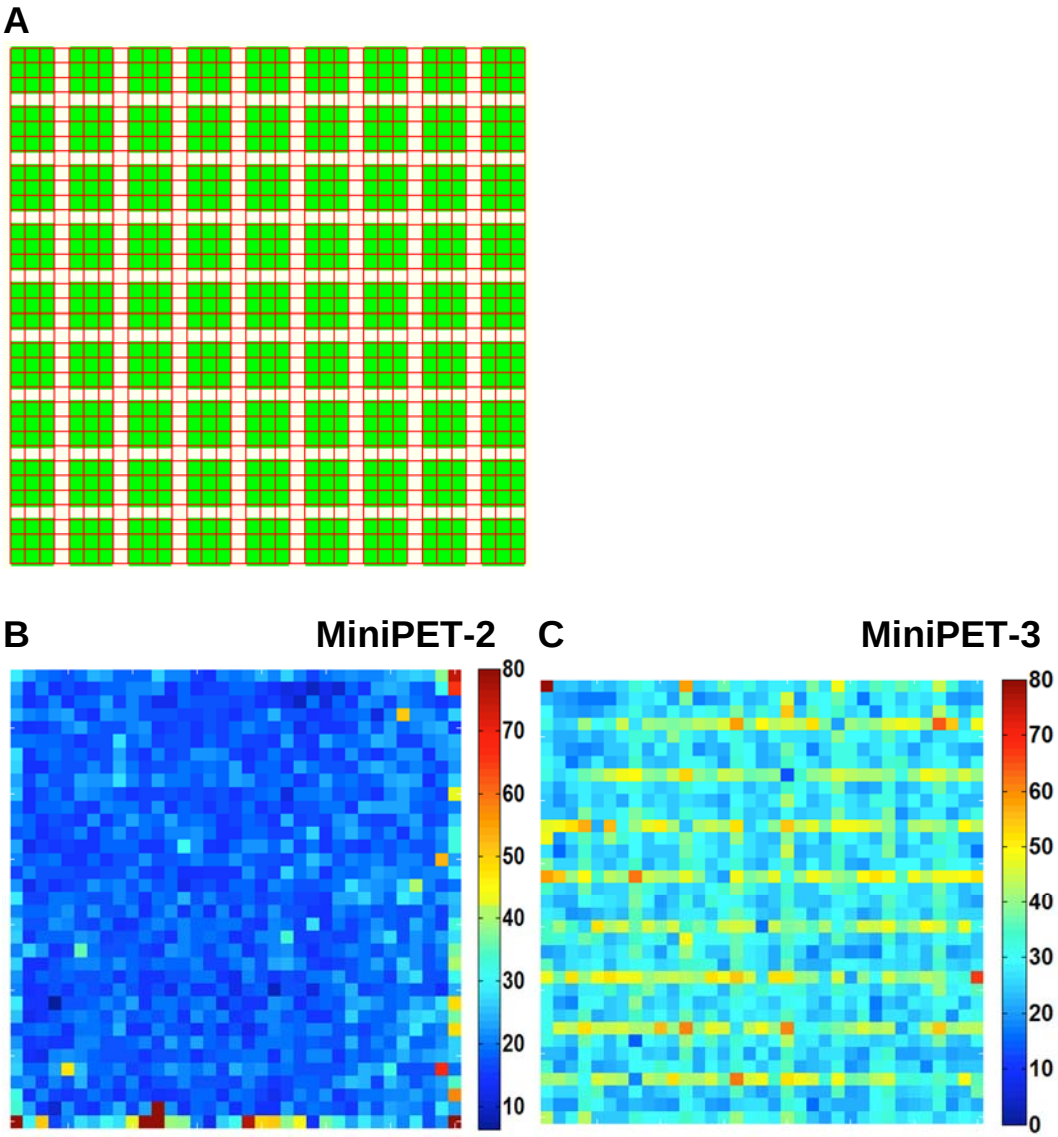

FIGURE 1. LYSO Scintillation Crystal (red) and SiPM sensor (green) overlap positions in the MiniPET-3 detector module (A). Energy resolution maps of the MiniPET-2 scanner (B) and the MiniPET-3 scanner (C) are displayed.

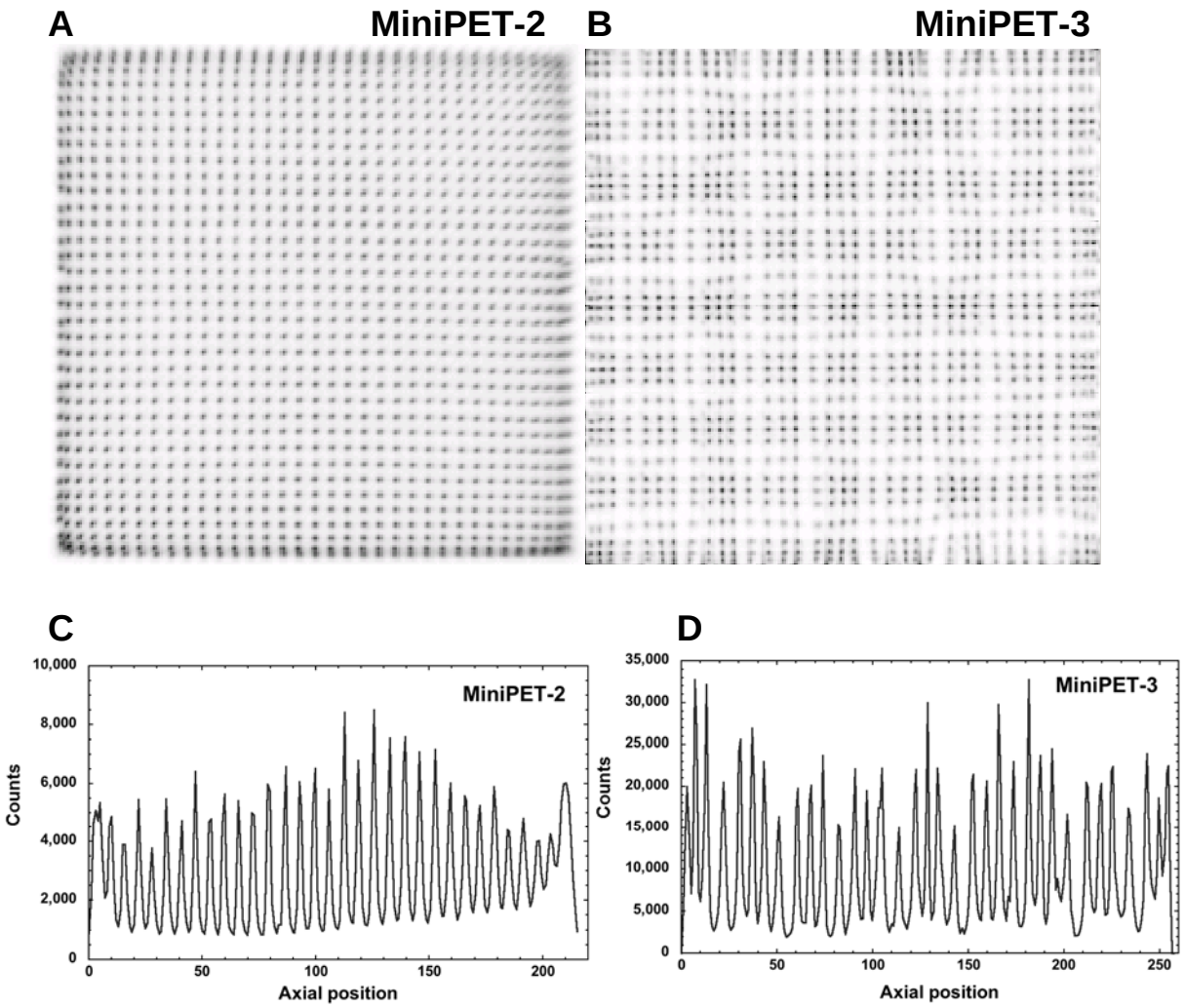

FIGURE 2. Position maps and line profiles of the MiniPET-2 (A, C) and the MiniPET-3 scanners (B, D).

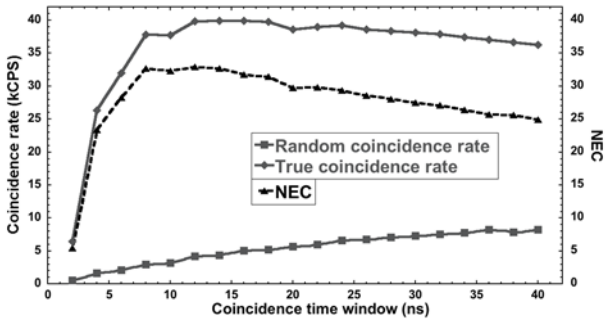

FIGURE 3. Coincidence Timing Window dependence on Random, True and NEC-like ($True^2$/(True+2*Random)) count rates for the MiniPET-3.

A

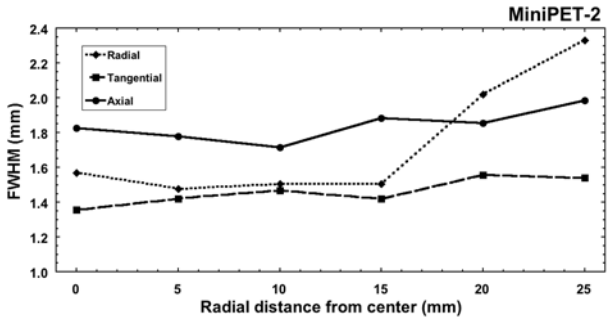

B

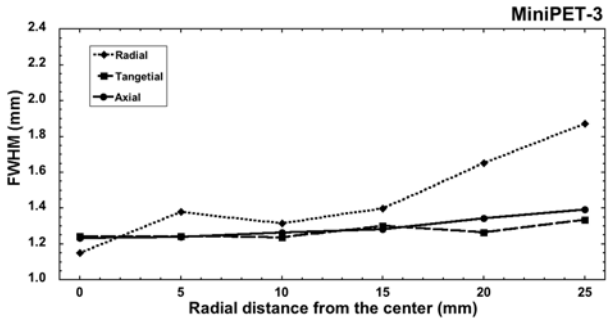

FIGURE 4. Dependence of the FWHM values on the radial distance, at the ¼ from the axial center for the MiniPET-2 (A) and the MiniPET-3 (B) scanners.

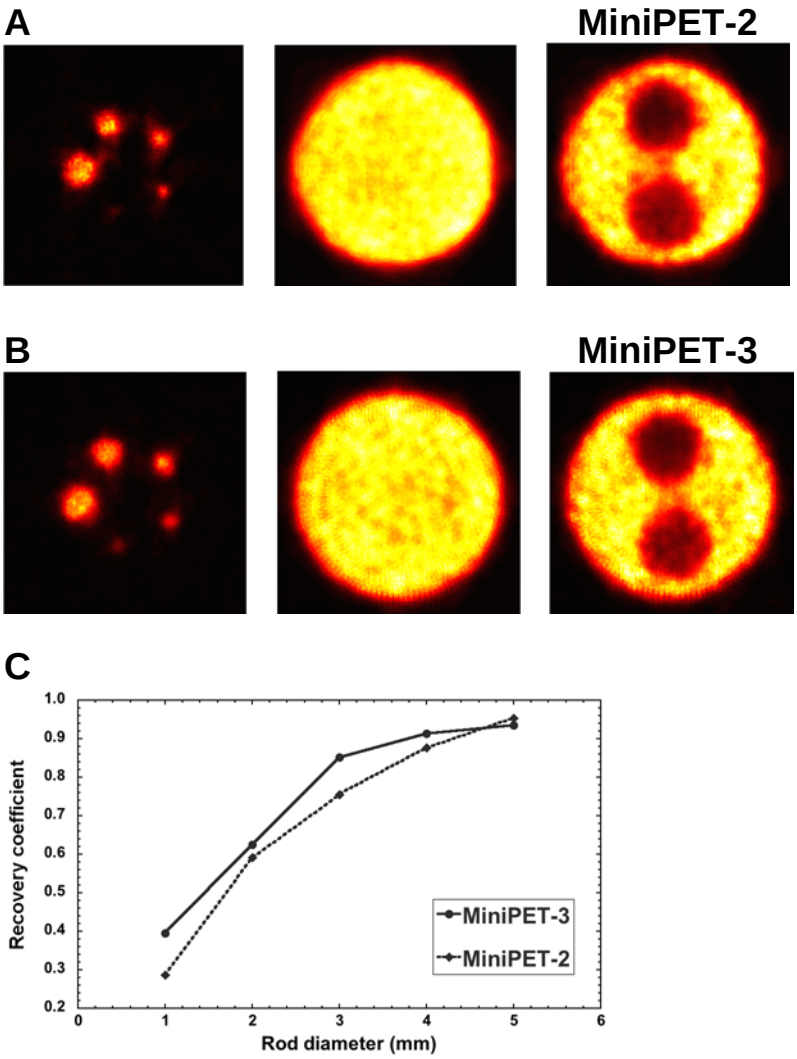

FIGURE 5. The reconstructed images of the NEMA NU 4 Image Quality phantom for the MiniPET-2 (A) and MiniPET-3 (B) scanners. The corresponding RC dependences on the rod radius for the both scanners are also displayed(C).

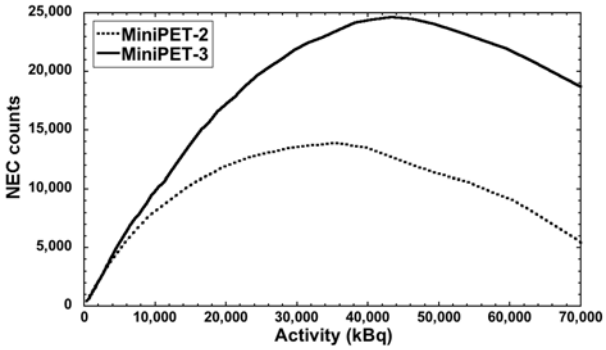

FIGURE 6. NEC Count rate performance results measured with the NEMA NU 4 rat phantom for the MiniPET-2 and MiniPET-3 scanners.

TABLE 1.
Basic physical and technical parameters of the MiniPET-2 and MiniPET-3 detector systems.

Category	MiniPET-2 (*12*)	MiniPET-3
Detector module		
Scintillator Material	LYSO	LYSO
Crystal Size (mm^3)	1.27×1.27×12	1.27×1.27×12
Crystal pitch (mm)	1.347	1.347
Crystal array size	35×35	35×35
Photon sensor	***PMT***, Hamamatsu	***SiPM***, ST Microelectronics
System		
Number of detector modules	12	12
Number of detector rings	35	35
Inner diameter of detector ring (mm)	211	211
Solid angle / 4π	0.22	0.22
Axial FOV (mm)	48	48
Trans-axial FOV (mm)	100	100

TABLE 2.
Sensitivity and spatial resolution data for both MiniPET systems.

Category	MiniPET-2	MiniPET-3
Energy window (keV)	350-650	360-662
Coincidence time window (ns)	6.0	8.0
Spatial resolution at ¼ CFOV		
Tangential (mm)	1.36	1.24
Radial (mm)	1.57	1.15
Axial (mm)	1.83	1.23
Sensitivity		
Peak absolute sensitivity (%)	1.37	1.36
Total absolute sensitivity (%)	0.6	0.7
Image Quality		
Uniformity (%STD)	5.59	6.49
SOR air	0.15	0.14
SOR water	0.26	0.24
Count Rate Performance		
NEC-Peak (rat phantom)	14 kcps (at 36 MBq)	24 kcps (at 43 MBq)
NEC-Peak (mouse phantom)	55 kcps (39 MBq)	91 kcps (at 44 MBq)
Scatter Fraction (rat phantom)	17.4%	16.1%
Scatter Fraction (mouse phantom)	5.6%	4.8%